

Hybridized-Mode Parametric Amplifier in Kinetic-Inductance Circuits

Danial Davoudi,¹ Abdul Mohamed,¹ and Shabir Barzanjeh^{1,*}

¹*Institute for Quantum Science and Technology, and Department of Physics and Astronomy,
University of Calgary, Department of Physics and Astronomy,
University of Calgary, Calgary, AB T2N 1N4 Canada*

(Dated: December 4, 2025)

Parametric amplification is essential for quantum measurement, enabling the amplification of weak microwave signals with minimal added noise. While Josephson-junction-based amplifiers have become standard in superconducting quantum circuits, their magnetic sensitivity, limited saturation power, and sub-kelvin operating requirements motivate the development of alternative nonlinear platforms. Here we demonstrate a two-mode kinetic-inductance parametric amplifier based on a pair of capacitively coupled Kerr-nonlinear resonators fabricated from NbTiN and NbN thin films. The distributed Kerr nonlinearity of these materials enables nondegenerate four-wave-mixing amplification with gains approaching 40 dB, gain-bandwidth products up to 6.9 MHz, and 1-dB compression powers two to three orders of magnitude higher than those of state-of-the-art Josephson amplifiers. A coupled-mode theoretical model accurately captures the pump-induced modification of the hybridized modes and quantitatively reproduces the observed signal and idler responses. The NbN device exhibits a significantly larger Kerr coefficient and superior gain-bandwidth performance, highlighting the advantages of high-kinetic-inductance materials. Our results establish coupled kinetic-inductance resonators as a robust platform for broadband, high-power, and magnetically resilient quantum-limited amplification, offering a scalable route for advanced readout in superconducting qubits, spin ensembles, quantum dots, and other microwave-quantum technologies.

I. INTRODUCTION

Many of the most sensitive quantum-measurement platforms rely on amplifying extremely weak electromagnetic fields without degrading the signal with additional noise. Parametric amplification provides this capability by driving a nonlinear medium with a strong pump tone, redistributing pump energy coherently into a signal and its corresponding idler. With appropriate engineering of the nonlinear medium and pump conditions, this process enables high gain and low added noise approaching the fundamental quantum limit in optical and microwave domains [1, 2]. In superconducting circuits, parametric amplifiers supply the ultra-low-noise gain required to extract weak microwave signals from quantum devices while adding only the minimum noise dictated by quantum mechanics [3–10]. They also generate nonclassical radiation, including squeezed states of light [11–13], and their noise performance and phase control are critical for fast, high-fidelity, single-shot readout in superconducting qubits [14], quantum dot qubits [15], and spin ensembles [16, 17]. Beyond qubit readout, parametric amplifiers play an important role in weak-measurement protocols [18, 19] and sensing [20–27].

For more than a decade, Josephson junctions have served as the primary nonlinear elements for realizing quantum-limited amplifiers (QLAs) [28, 29]. Their implementations fall into two main families, cavity-based Josephson parametric amplifiers (JPAs) [30] and traveling-wave Josephson parametric amplifiers (JTWPAs) [31, 32]. Both rely on the strong nonlinearity

of Josephson junctions to support three-wave mixing (3WM) [33–35] or four-wave mixing (4WM) [36, 37]. Despite outstanding performance, these devices face fundamental limitations, including susceptibility to magnetic parasitic noise [38], modest power-handling capability, and operational constraints that typically require sub-kelvin temperatures to maintain coherence and stability [9, 39]. These restrictions motivate the exploration of alternative nonlinear platforms that offer increased robustness and greater operational flexibility.

Superconducting thin films with strong kinetic inductance provide such an alternative [33, 35, 40–44]. Materials such as niobium–titanium–nitride (NbTiN) [35, 37, 45], niobium nitride (NbN) [34, 46], titanium nitride (TiN) [47], and granular aluminum (grAl) [48] exhibit a spatially uniform Kerr-type nonlinearity that enables strong four-wave mixing without the need for Josephson junctions. Kinetic-Inductance Parametric Amplifiers (KIPAs) built from these materials demonstrate high resilience to magnetic noise [45, 49], substantially higher saturation powers [35, 37], and operation at higher temperatures due to their high critical temperatures [35, 50]. These characteristics make KIPAs attractive for multiplexed readout of large-scale quantum processors without extensive magnetic shielding [36] and enable amplifier operation in a broader temperature range, improving practicality for scalable quantum technologies.

In this work, we develop a nonlinear microwave amplification platform based on two coupled kinetic-inductance resonators. Through a combination of theoretical modeling and experimental measurements, we demonstrate nondegenerate two-mode amplification driven by four-wave mixing in NbN and NbTiN thin films. By engineering the coupling between the resonators and opti-

* shabir.barzanjeh@ucalgary.ca

mizing the pump frequency and amplitude, the system operates as a two-mode amplifier in which the signal and idler occupy well-separated spectral modes. This architecture combines the advantages of distributed kinetic-inductance nonlinearity, magnetic robustness, and high operational temperature with the design flexibility of multimode resonators [51–53]. The resulting platform expands the design space for quantum-limited amplifiers and offers a scalable route to broadband, high-power, and magnetically resilient amplification for next-generation quantum technologies.

II. THEORETICAL MODEL FOR TWO-MODE AMPLIFICATION

In this section, we develop the theory of two-mode amplification based on four-wave mixing process. The system, shown schematically in Fig. 1(a), consists of two coupled Kerr-nonlinear ($\chi^{(3)}$) resonators with coupling rate g . Each resonator has a resonance frequency ω_j and is characterized by extrinsic and intrinsic damping rates $\kappa_{e,j}$ and $\kappa_{i,j}$ for $j = 1, 2$. This coupled nonlinear resonators system can be described by the Hamiltonian ($\hbar = 1$)

$$H = \sum_{j=1,2} \omega_j a_j^\dagger a_j + g(a_1 a_2^\dagger + a_2 a_1^\dagger) + \sum_{j=1,2} \frac{K_j^0}{2} [(a_j^\dagger)^2 a_j^2], \quad (1)$$

where a_j are the annihilation operators for resonators $j = 1, 2$. The first term in the Hamiltonian describes the two uncoupled resonators with frequencies ω_j , the second term shows the coherent photon exchange at rate g , and the third term represents the self-Kerr nonlinearity arising from the Kerr ($\chi^{(3)}$) medium in each resonator with Kerr coefficient K_j^0 . For simplicity, we assume a symmetric nonlinear regime with $K^0 = K_1^0 = K_2^0$.

The dynamics of the system are described by the quantum Langevin equations

$$\begin{aligned} \frac{da_1}{dt} &= -\left[i\omega_1 + \frac{\kappa_1}{2}\right] a_1 - ig a_2 - i\frac{K_1^0}{2} a_1^\dagger a_1^2 \\ &\quad + \sqrt{\kappa_{e,1}} [a_p + a_{e,1}] + \sqrt{\kappa_{i,1}} a_{i,1}, \\ \frac{da_2}{dt} &= -\left[i\omega_2 + \frac{\kappa_2}{2}\right] a_2 - ig a_1 - i\frac{K_2^0}{2} a_2^\dagger a_2^2 \\ &\quad + \sqrt{\kappa_{e,2}} [a_p + a_{e,2}] + \sqrt{\kappa_{i,2}} a_{i,2}, \end{aligned} \quad (2)$$

where $\kappa_j = \kappa_{e,j} + \kappa_{i,j}$ is the total damping rate of each resonator with $j = 1, 2$. These equations incorporate the quantum noise entering via the external port (a_e , associated with the extrinsic damping rate κ_e) and the intrinsic losses of each resonator mode (a_i , associated with the intrinsic rate κ_i). The corresponding noise correlations are

$$\begin{aligned} \langle a_{e(i)}(t) a_{e(i)}^\dagger(t') \rangle &= \langle a_{e(i)}^\dagger(t) a_{e(i)}(t') \rangle + \delta(t - t') \\ &= (\bar{n}_{e(i)} + 1) \delta(t - t'), \end{aligned} \quad (3)$$

where $\delta(t)$ is the Dirac delta function and $\bar{n}_{e(i)}$ is the thermal Planck occupancy of the corresponding bath.

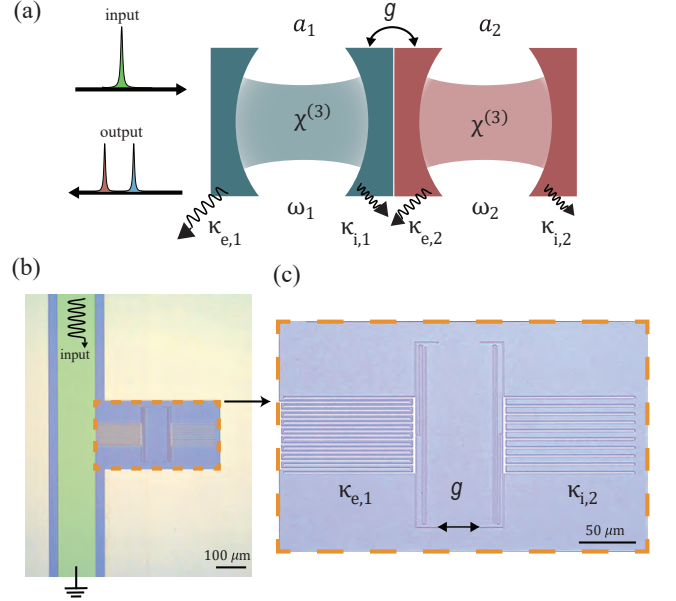


FIG. 1: (a) Schematic of the coupled-resonator system used for two-mode amplification. The device consists of two Kerr-nonlinear ($\chi^{(3)}$) resonators with bare frequencies $\omega_{1,2}$, coupled coherently at rate g . Each resonator exchanges energy with a common transmission line through an external damping channel $\kappa_{e,j}$ and experiences intrinsic dissipation $\kappa_{i,j}$. The intrinsic Kerr nonlinearity provides the effective $\chi^{(3)}$ response required for four-wave mixing, enabling the generation of signal and idler fields under pump drive. (b) False-color optical image of the implementation of the actual coupled kinetic-inductance amplifier. The green area shows the coplanar transmission line, and the yellow color areas exhibit the ground plane. Two Kerr-nonlinear LC resonators, realized using NbTiN or NbN nanowire inductors and U-shaped shunt capacitors, are capacitively coupled at rate g and driven through an interdigitated capacitor fed by a coplanar transmission line. The kinetic-inductance nonlinearity of the thin films provides the $\chi^{(3)}$ response needed for four-wave-mixing amplification. (c) Zoomed-in image of coupled resonators.

The term a_p shows the pump field injected into the system, required to generate two-mode amplification. In the strong-pump regime, pump fluctuations can be ignored, and the pump may therefore be treated as a classical field with amplitude $a_p \rightarrow \alpha_p = |\alpha_p|e^{-i\omega_p t}$. Under this assumption, the pump dynamics can be eliminated, allowing us to linearize Eqs. (2) by writing $a_j = \alpha_j + \delta a_j$, where δa_j denotes the fluctuation operator around the steady-state amplitude α_j in each resonator. In this regime, quadratic and higher-order quantum fluctuations can be neglected and the equations of motion can be simplified.

Transforming into a frame rotating at the pump frequency ω_p , the linearized fluctuations around the classical steady state are collected in the vector $\mathbf{A} =$

$[\delta a_1, \delta a_1^\dagger, \delta a_2, \delta a_2^\dagger]^T$. We assume that resonator 2 is only weakly coupled to the input line, such that $\kappa_{e,1} \gg \kappa_{e,2}$. In this regime, neither the pump nor the fluctuations entering through the weakly coupled port appreciably modify the system dynamics, allowing the terms proportional to $\sqrt{\kappa_{e,2}}[a_p + a_{e,2}]$ in Eqs. (2) to be safely ignored. As shown later, this approximation is well supported by the parameters of our superconducting circuit. Under these conditions, the equations of motion simplify and can be written in the compact form

$$\frac{d\mathbf{A}}{dt} = \mathbf{\Gamma} \mathbf{A} + \sqrt{\kappa_{e,1}} \mathbf{A}_e + \mathbf{A}_i, \quad (4)$$

where $\mathbf{A}_e = [\delta a_{e,1}, \delta a_{e,1}^\dagger, 0, 0]^T$, and $\mathbf{A}_i = [\sqrt{\kappa_{i,1}} \delta a_{i,1}, \sqrt{\kappa_{i,1}} \delta a_{i,1}^\dagger, \sqrt{\kappa_{i,2}} \delta a_{i,2}, \sqrt{\kappa_{i,2}} \delta a_{i,2}^\dagger]^T$, with

$$\mathbf{\Gamma} = \begin{bmatrix} -i\Delta_1 - \frac{\kappa_1}{2} & -iK_1 & -ig & 0 \\ iK_1^* & i\Delta_1 - \frac{\kappa_1}{2} & 0 & ig \\ -ig & 0 & -i\Delta_2 - \frac{\kappa_2}{2} & -iK_2 \\ 0 & ig & iK_2^* & i\Delta_2 - \frac{\kappa_2}{2} \end{bmatrix}, \quad (5)$$

being the drift matrix, in which $\Delta_j = \omega_j - \omega_p + 2|K_j|$ is the pump-shifted detuning and $K_j = \frac{K_0}{2} \alpha_j^2$ is the effective Kerr coefficient that depends on the intracavity photon number $n_j = |\alpha_j|^2$. The amplitudes α_j follow from the coupled nonlinear steady-state equations

$$\begin{aligned} \left[i\Delta_1 + \frac{\kappa_1}{2}\right]\alpha_1 + ig\alpha_2 + \frac{i|\alpha_1|^2\alpha_1}{2} &= \sqrt{\kappa_{e,1}}\alpha_p, \quad (6) \\ \left[i\Delta_2 + \frac{\kappa_2}{2}\right]\alpha_2 + ig\alpha_1 + \frac{i|\alpha_2|^2\alpha_2}{2} &= 0. \end{aligned}$$

Solving these equations numerically yields the steady-state photon numbers in each resonator, from which the Kerr coefficients K_j are obtained directly. The steady-state Eqs. (6) generally have multiple solutions. To determine which solutions are physically realized, we analyze the eigenvalues of the drift matrix (5). According to the Routh–Hurwitz criterion [54], a steady state is dynamically stable only when every eigenvalue has a negative real part, ensuring that small perturbations decay. If any eigenvalue acquires a positive real part, the corresponding steady state becomes unstable and cannot be sustained.

By having the steady-state amplitudes, we can solve Eq. (4) in the Fourier domain and obtain the intra-cavity operators. By substituting the solutions into the corresponding input-output relation i.e., $a_{\text{out}} = \sqrt{\kappa_{e,1}}\delta a_1 - a_{e,1}$, we obtain

$$a_{\text{out}} = \sqrt{G_S(\omega)}\delta a_{e,1}(\omega) + \sqrt{G_I(\omega)}\delta a_{e,1}^\dagger(-\omega) + A_{\text{noise}}, \quad (7)$$

where $G_S(\omega) = \kappa_{e,1} \mathcal{G}_{11}(\omega)$ and $G_I(\omega) = \kappa_{e,1} \mathcal{G}_{12}(\omega)$, with $\mathcal{G}(\omega) = (-i\omega \mathbf{I} - \mathbf{\Gamma})^{-1}$ in which \mathbf{I} is the identity

matrix. Here, the operator A_{noise} comes from intrinsic losses and contains the corresponding fluctuation operators $a_{i,1(2)}$. In the ideal case where the intrinsic losses vanish, this term can be neglected.

Equation (7) has the standard form of a parametric amplifier [1, 3]. The first term describes signal amplification with gain G_S and the second term gives the corresponding idler amplification with gain G_I . The spectral locations of the signal and idler depend on the chosen pump frequency. A better understanding of the underlying two-mode amplification process is obtained by working in the hybridized-mode picture. The coherent coupling between the two resonators mixes them into symmetric and antisymmetric normal modes with eigenfrequencies $\omega_{\pm} = \frac{\omega_1 + \omega_2 \pm \sqrt{4g^2 + (\omega_1 - \omega_2)^2}}{2}$, in which both hybridized modes couple to the common transmission line used for pumping and readout. At the anticrossing point $\omega_1 = \omega_2$ the hybridized modes are split by $\omega_+ - \omega_- = 2g$. When the system is driven at the midpoint between the hybridized modes, $\omega_p = \frac{\omega_+ + \omega_-}{2} = g$, Eq. (7) simplifies to $a_{\text{out}} \propto \sqrt{G_S} \delta a_{e,1}(g) + \sqrt{G_I} \delta a_{e,1}^\dagger(-g)$. This expression shows that the amplification takes place at the frequencies of the hybridized normal modes of the coupled-resonator system. Note that all frequencies are defined in the frame rotating at the pump frequency.

III. EXPERIMENT

A. Design and fabrication

The theoretical framework developed above can be implemented experimentally using kinetic-inductance thin films such as NbTiN and NbN, which naturally support two-mode amplification through a 4WM interaction between a pair of spectrally distinct microwave resonators. The key physical mechanism is the current-dependent kinetic inductance of the superconducting film, $L_k(I) = L_0 \left[1 + \left(\frac{I}{I^*}\right)^2\right]$, where L_0 is the zero-bias kinetic inductance and I^* is a material-dependent scale set by the critical current [43, 55–57]. The resulting quadratic dependence $L_k \propto I^2$ provides an effective Kerr ($\chi^{(3)}$) nonlinearity that mediates the 4WM process responsible for parametric gain [45], see Appendices B.

To harness this nonlinearity, the device incorporates two Kerr-nonlinear LC resonators with bare frequencies $\omega_{1,2}$, coupled capacitively at a coherent rate g , as shown in Fig. 1(b) and (c). A coplanar transmission line delivers the microwave pump to an interdigitated capacitor (IDC), which drives both resonators simultaneously. Each mode is realized as a compact lumped-element circuit formed by a meandered nanowire inductor—providing the kinetic inductance—placed in parallel with a U-shaped shunt capacitor.

We implemented this architecture using superconducting NbTiN and NbN films, each 10 nm thick and deposited on high-resistivity silicon substrates (500 μm).

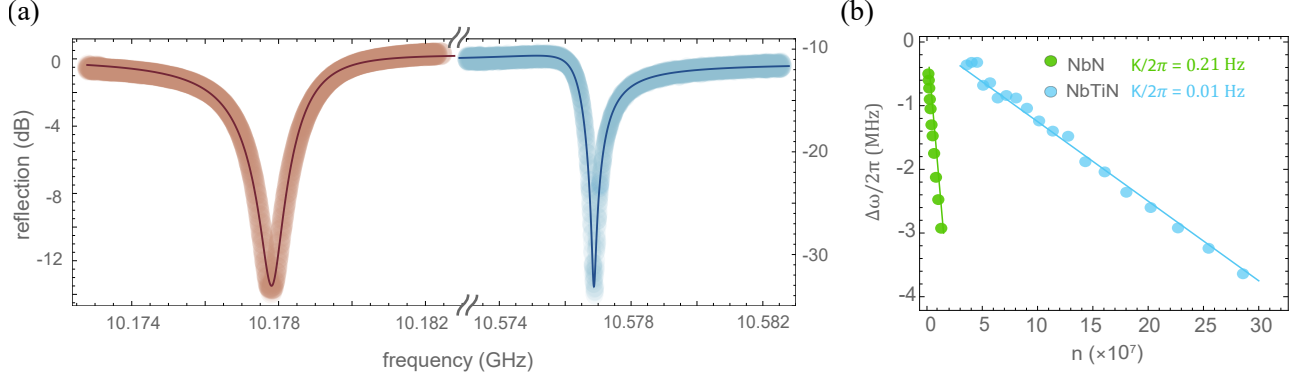


FIG. 2: (a) Reflection spectrum of the NbTiN device showing two hybridized modes at $\omega_-/2\pi = 10.178$ GHz and $\omega_+/2\pi = 10.577$ GHz, corresponding to a mode splitting of $(2g)/2\pi \simeq 434$ MHz. The asymmetric coupling of the bare resonators results in different external linewidths for the two hybridized modes. (b) Self-Kerr shift of the hybridized modes extracted from the resonance frequency shift $\Delta\omega$ versus intracavity photon number n . The slopes yield Kerr coefficients of $K/2\pi \approx 0.01$ Hz for NbTiN and $K/2\pi \approx 0.21$ Hz for NbN using $1\ \mu\text{m}$ -wide nanowires, with the larger Kerr in NbN reflecting its higher kinetic-inductance participation.

Fabricating identical circuit layouts in both materials enabled a direct comparison of their nonlinear response and achievable amplification. The nanowire inductors and shunt capacitors were designed to maximize the kinetic-inductance participation ratio L_K/L_T , where L_T is the total circuit inductance, thereby enhancing the Kerr coefficient K . Additional fabrication details are provided in the Appendices.

Figure 2(a) shows the reflection spectrum of the NbTiN device, which features two well-resolved hybridized modes at $\omega_-/2\pi = 10.178$ GHz and $\omega_+/2\pi = 10.577$ GHz. These frequencies correspond to a mode splitting $(2g)/2\pi \simeq 434$ MHz. Because the two bare resonators are detuned, the hybridized modes couple asymmetrically to the transmission line, resulting in different external linewidths,

$$\kappa_{\pm} = \frac{\kappa_1 + \kappa_2}{2} \left(1 \pm \frac{(\omega_1 - \omega_2)/g}{2\sqrt{4 + [(\omega_1 - \omega_2)/g]^2}} \right). \quad (8)$$

In our devices, the extracted effective damping rates using the single-port theory model for NbTiN are ($\kappa_{e,1}/2\pi = 1.40$ MHz, $\kappa_{i,1}/2\pi = 0.91$ MHz), ($\kappa_{e,2}/2\pi = 0.64$ MHz, $\kappa_{i,2}/2\pi = 0.65$ MHz), while for NbN they are ($\kappa_{e,1}/2\pi = 2.3$ MHz, $\kappa_{i,1}/2\pi = 1.1$ MHz), ($\kappa_{e,2}/2\pi = 0.3$ MHz, $\kappa_{i,2}/2\pi = 0.9$ MHz). The reflection data also allow us to extract the self-Kerr nonlinearity of the circuit modes. To determine the Kerr coefficient, we measure the resonance shift as a function of the intracavity photon number n_j , where the slope yields $K_j = \Delta\omega_j/n_j$ for each mode $j = 1, 2$. As shown in Fig. 2(b), the extracted values are $K/2\pi \approx 0.01$ Hz for NbTiN and $K/2\pi \approx 0.21$ Hz for NbN, obtained using $1\ \mu\text{m}$ -wide nanowires. The larger Kerr coefficient in NbN is consistent with the expected scaling $K \propto \omega^2 A^{-3} (L_K/L_T)^2$, where A is the nanowire

cross-sectional area and L_K/L_T is the kinetic-inductance participation ratio [47, 58].

B. Two-mode amplification

To observe amplification, the circuit is driven with a pump tone placed midway between the two hybridized modes, $\omega_p = (\omega_+ + \omega_-)/2$. This choice of pump frequency activates a 4WM process that converts pump photons into signal and idler fields appearing at the symmetric and antisymmetric hybridized modes. Under these conditions, the device operates as a non-degenerate, phase-insensitive parametric amplifier.

For the NbTiN device, Fig. 3(a) shows the measured signal and idler gain as a function of the detuning with respect to the resonators' central frequency at different applied pump powers. The amplifier reaches nearly $G = 40$ dB of gain at a pump power of approximately -23 dBm at the device input. To identify the optimal operating point, we sweep both the pump frequency and pump power, mapping out the conditions that maximize the non-degenerate gain. The solid curves in Fig. 3(a) represent the theoretical model introduced in Eq. (7), evaluated using independently extracted device parameters, and provide excellent fits to the experimental data. The two contour-plot insets in Fig. 3(a) display the amplification landscape as a function of pump frequency and detuning for both the signal and the idler. As shown in the Appendices, we performed the same measurement on the NbN device and observed comparable performance, reaching nearly 40 dB of gain at a pump power of about -36 dBm at the device input.

Figure 3(b) presents the gain-bandwidth product, $\text{GBP} = \sqrt{G}\Gamma$, where Γ is the full width at half maximum (FWHM) of the gain profile, plotted as a function

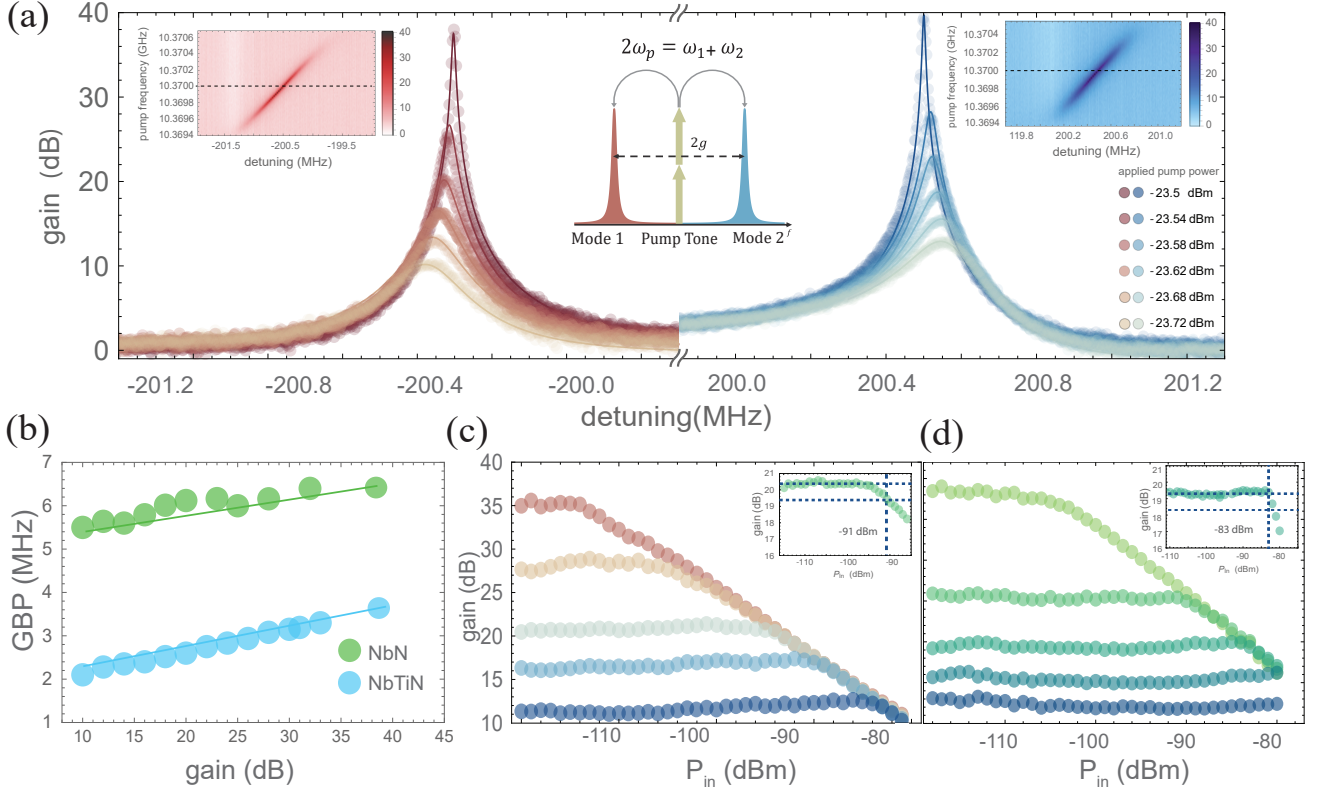


FIG. 3: (a) Signal and idler gain versus detuning for the NbTiN device at several pump powers. Maximum gain approaches 40 dB at a pump power of -23 dBm, with solid curves showing fits to the theoretical model. (b) Gain-bandwidth product (GBP) as a function of gain for NbTiN and NbN devices. The NbTiN device reaches $\text{GBP} = 3.3$ MHz, while NbN reaches $\text{GBP} = 6.9$ MHz, consistent with its larger Kerr nonlinearity. Power-saturation characteristics for NbTiN (c) and NbN (d). The 1-dB compression points occur near $P_{in} \approx -91$ dBm (NbTiN) and -83 dBm (NbN) at 20 dB gain, demonstrating saturation powers two to three orders of magnitude higher than typical Josephson-junction-based amplifiers.

of the amplifier gain G for both NbTiN and NbN devices. From these measurements we obtain $\text{GBP} = 3.3$ MHz for NbTiN and $\text{GBP} = 6.9$ MHz for NbN at around 40 dB gain, demonstrating that the NbN device provides better gain-bandwidth performance than the NbTiN. Note that, theoretically, the gain-bandwidth product follows $\sqrt{G} \Gamma = \frac{\kappa_+ + \kappa_-}{\kappa_+ + \kappa_-}$ [3], which identifies the parameter regime in which the GBP can be optimized for a given amplifier gain.

Fig. 3(c)–(d) shows the power-saturation behavior of the NbTiN and NbN devices as a function of the input probe power P_{in} . The 1-dB compression points occur at $P_{in} \approx -83$ dBm for NbN and $P_{in} \approx -91$ dBm for NbTiN at a gain of approximately 20 dB. These measurements demonstrate a two-to-three-orders-of-magnitude improvement in power handling compared with state-of-the-art Josephson-junction-based quantum-limited amplifiers [39, 59, 60].

We finally note that, in the present devices, the pump frequency is applied near to the two hybridized modes. Therefore, a significant fraction of the strong pump reflects back toward the input port and saturates the subse-

quent amplification chain (HEMT and room-temperature amplifiers). This prevents a reliable determination of the added-noise performance and precludes an accurate extraction of the noise contribution of the 4WM two-mode amplifier. Based on measurements in closely related architectures operating in the three-wave-mixing regime, we expect the added noise to be below one quantum at the signal input [35].

IV. CONCLUSION AND OUTLOOK

We have demonstrated a coupled-mode kinetic-inductance parametric amplifier that provides two-mode, non-degenerate gain through a four-wave-mixing process in NbTiN and NbN nanowire resonators. The combination of Kerr-nonlinear circuit design and the intrinsic, distributed nonlinearity of kinetic-inductance films enables strong parametric gain approaching 40 dB, gain-bandwidth products in the megahertz regime, and saturation powers that exceed those of Josephson-junction-based amplifiers by several

orders of magnitude. The NbN device, in particular, exhibits a larger Kerr coefficient and improved gain–bandwidth performance, consistent with its higher kinetic-inductance participation. Our coupled-mode theory captures the essential features of the amplification process, including pump-induced modification of the hybridized modes and the emergence of signal and idler tones at the symmetric and antisymmetric resonances. The close agreement between model and measurement confirms the validity of this framework and provides clear guidance for optimizing future device geometries.

Looking ahead, increasing the kinetic-inductance participation—for example by using narrower nanowires or materials with stronger nonlinearity such as TiN or granular aluminum—and reducing internal losses through improved film growth should further enhance gain and bandwidth. More advanced coupling networks may also enable broader impedance matching and increased dynamic range.

Kinetic-inductance parametric amplifiers of the type demonstrated here offer a promising pathway toward scalable, high-dynamic-range quantum signal processing. Their resilience to magnetic noise, high saturation power, and elevated-temperature operation make them well suited for multiplexed readout in superconducting-qubit, spin, and quantum-dot platforms, as well as broadband sensing and microwave quantum optics. As quantum systems grow in size and complexity, the advantages of kinetic-inductance-based amplification are likely to become increasingly important.

ACKNOWLEDGMENT

We acknowledge funding by the Natural Sciences and Engineering Research Council of Canada (NSERC) through its Discovery Grant and Quantum Alliance Grant, and NSERC through Advance Grant project, and Alliance Quantum Consortium. This project is funded [in part] by the Government of Canada. Ce projet est financé [en partie] par le gouvernement du Canada.

APPENDICES

Appendix A: Fabrication Recipe

The devices are fabricated using a straightforward single-step optical-lithography process. A ten-nanometre superconducting thin film of niobium–titanium–nitride or niobium–nitride is deposited on a five-hundred-micrometre, high-resistivity silicon wafer by atomic-layer deposition. A protective layer of polymethyl methacrylate (PMMA A8) is applied to shield the film during dicing into ten-by-ten-millimetre chips. Each chip is first cleaned in acetone and isopropyl alcohol in a sonication bath, then prebaked and coated with AZ1529 photoresist, producing a film thickness of

approximately three micrometres before a soft bake at one hundred degrees Celsius. The patterns are written using a maskless optical lithography system, after which the exposed regions are developed in AZ 400K solution diluted at a ratio of one to four and subsequently rinsed in deionized water. The structures are then transferred into the superconducting film by a six-minute etch in an inductively coupled plasma reactor using sulphur hexafluoride, argon, and trifluoromethane gases. Finally, the chips are exposed to ultraviolet light to remove any residual resist and cleaned again in acetone to complete the process.

After fabrication, the chips are mounted in an oxygen-free-high-conductivity copper sample enclosure using silver paste to ensure good thermal anchoring to the ten-millikelvin stage. Microwave connections are made by bonding the on-chip launch pads, designed with fifty-ohm impedance, to the printed circuit board using aluminium wire bonds and surface-mount connectors. Additional wire bonds between the on-chip ground planes and the printed circuit board ground are added to eliminate charge build-up and to ensure stable electrical performance during cryogenic operation.

Appendix B: Enhancement of the Nonlinear Response

The total inductance of a superconducting nanowire contains both a geometric (magnetic) contribution and a kinetic contribution, $L_T = L_M + L_K$. The geometric component is set by the physical layout of the conductor and reflects the energy stored in the magnetic field generated by the current. The kinetic inductance, by contrast, originates from the inertia of Cooper pairs and becomes significant in thin, high-resistivity superconducting films where the relaxation time is long. Enhancing this kinetic contribution is key to increasing the nonlinear response of the resonator and reducing the pump power required to reach the amplification regime.

For a nanowire with length l , width w , and thickness t , the kinetic inductance can be obtained by equating the kinetic energy of the Cooper pairs to the inductive energy. Within Bardeen–Cooper–Schrieffer theory, and for films thinner than the penetration depth, the kinetic inductance takes the form

$$L_K = \frac{\hbar \rho l}{\pi \Delta_0 w t},$$

where ρ is the normal-state resistivity and Δ_0 is the superconducting energy gap [61]. This expression shows that narrower, thinner, and longer nanowires yield larger kinetic inductance and therefore stronger nonlinear response.

The Kerr coefficient quantifies the resonance frequency shift per intracavity photon. Using the quantized nonlinear resonator model, the coefficient can be expressed as

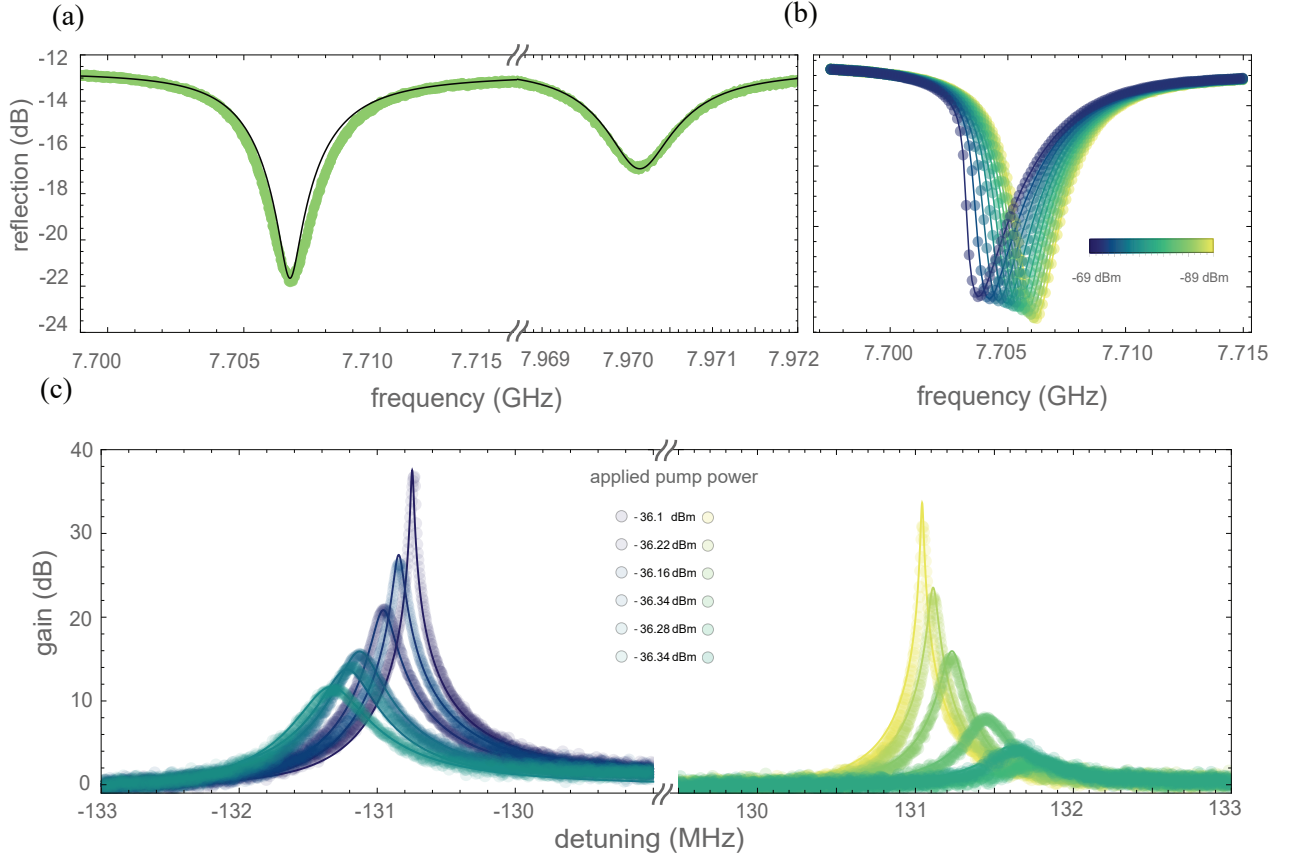


FIG. 4: (a) Frequency response measured in reflection for the coupled NbN resonators. (b) Kerr shift of the ω_- mode obtained by driving the resonator with a strong signal tone. (c) Two-mode amplification observed when the device is driven with a pump tone placed midway between the hybridized modes. Dotted curves show measured data fitted using Eq. 7.

[47]

$$K = \frac{3\hbar^3 \rho_n^2}{4N_0 \Delta_0^4 \pi^2} \frac{\omega l}{w L_T^2 t^3},$$

where N_0 is the density of states at the Fermi level, ω is the resonant frequency, and L_T is the total inductance. This expression makes clear that the Kerr coefficient increases with kinetic-inductance participation, higher resonant frequency, smaller cross-sectional area, and smaller superconducting energy gap. We extracted sheet inductances $L_{\square}^k = 103$ nH/ \square and $L_{\square}^k = 31$ nH/ \square for ten-nanometre-thick NbN and NbTiN films, respectively, by fitting the measured resonance frequencies of our designed single and coupled resonators using Sonnet electromagnetic (EM) simulations.

Motivated by these scalings, we implemented the amplifier design in niobium–nitride, a material with a smaller superconducting energy gap than ni-

bium–titanium–nitride [62]. This choice increases the kinetic inductance and strengthens the nonlinear response, allowing parametric amplification to be achieved with substantially lower pump power.

Appendix C: Amplification of NbN

The NbN device was characterized using the same methods described for the NbTiN sample. Reflection measurements shows two hybridized modes at 7.707 GHz and 7.970 GHz, from which the coupling rates were extracted via Lorentzian fits. Power-dependent measurements of the lower mode confirmed the expected Kerr-induced frequency shift. Driving the circuit with a pump tone located midway between the two hybridized modes generated non-degenerate signal and idler peaks. Increasing the pump power from -36.34 dBm to -36.10 dBm enhanced the parametric gain, reaching nearly 40 dB, as shown in Fig. 4(c).

[1] C. M. Caves, Quantum limits on noise in linear amplifiers, *Phys. Rev. D* **26**, 1817 (1982).

[2] B. R. Mollow, Quantum theory of parametric amplification. i, *Physical Review* **160**, 1076 (1967).

- [3] A. A. Clerk, M. H. Devoret, S. M. Girvin, F. Marquardt, and R. J. Schoelkopf, Introduction to quantum noise, measurement, and amplification, *Rev. Mod. Phys.* **82**, 1155 (2010).
- [4] J. Aumentado, Superconducting parametric amplifiers: the state of the art in josephson parametric amplifiers, *IEEE Microwave Magazine* **21**, 45 (2020).
- [5] A. Blais, A. L. Grimsmon, S. M. Girvin, and A. Wallraff, Circuit quantum electrodynamics, *Reviews of Modern Physics* **93**, 025005 (2021).
- [6] P. Krantz, M. Kjaergaard, F. Yan, T. P. Orlando, S. Gustavsson, and W. D. Oliver, A quantum engineer's guide to superconducting qubits, *Applied Physics Reviews* **6**, 021318 (2019).
- [7] N. Bergeal, F. Schackert, M. Metcalfe, R. Vijay, V. E. Manucharyan, L. Frunzio, D. E. Prober, R. J. Schoelkopf, S. M. Girvin, and M. H. Devoret, Phase-preserving amplification near the quantum limit with a josephson ring modulator, *Nature* **465**, 64 (2010).
- [8] M. Hatridge, R. Vijay, D. H. Slichter, J. Clarke, and I. Siddiqi, Dispersive magnetometry with a quantum limited squid parametric amplifier, *Phys. Rev. B* **83**, 134501 (2011).
- [9] M. A. Castellanos-Beltran and K. W. Lehnert, Widely tunable parametric amplifier based on a superconducting quantum interference device array resonator, *Appl. Phys. Lett.* **91**, 083509 (2007).
- [10] A. Bienfait, J. J. Pla, Y. Kubo, M. Stern, X. Zhou, C. C. Lo, C. D. Weis, T. Schenkel, M. L. W. Thewalt, D. Vion, D. Esteve, B. Julsgaard, K. Mølmer, J. J. L. Morton, and P. Bertet, Reaching the quantum limit of sensitivity in electron spin resonance, *Nature Nanotechnology* **11**, 253 (2016).
- [11] L. Zhong, E. P. Menzel, R. Di Candia, P. Eder, M. Ihmig, A. Baust, M. Haeberlein, E. Hoffmann, K. Inomata, T. Yamamoto, Y. Nakamura, E. Solano, F. Deppe, A. Marx, and R. Gross, Squeezing with a flux-driven josephson parametric amplifier, *New Journal of Physics* **15**, 125013 (2013).
- [12] C. Eichler, D. Bozyigit, C. Lang, L. Steffen, J. Fink, and A. Wallraff, Experimental state tomography of itinerant single microwave photons, *Phys. Rev. Lett.* **106**, 220503 (2011).
- [13] M. A. Castellanos-Beltran, K. D. Irwin, G. C. Hilton, L. R. Vale, and K. W. Lehnert, Amplification and squeezing of quantum noise with a tunable josephson metamaterial, *Nat. Phys.* **4**, 929 (2008).
- [14] T. Walter, P. Kurpiers, S. Gasparinetti, P. Magnard, A. Potočnik, Y. Salathé, M. Pechal, M. Mondal, M. Oppliger, C. Eichler, and A. Wallraff, Rapid, high-fidelity, single-shot dispersive readout of superconducting qubits, *Physical Review Applied* **7**, 054020 (2017).
- [15] J. Stehlik, Y.-Y. Liu, C. M. Quintana, C. Eichler, T. R. Hartke, and J. R. Petta, Fast charge sensing of a cavity-coupled double quantum dot using a josephson parametric amplifier, *Physical Review Applied* **4**, 014018 (2015).
- [16] W. Vine, M. Savytskyi, D. Parker, J. Slack-Smith, T. Schenkel, J. C. McCallum, B. C. Johnson, A. Morello, and J. J. Pla, In situ amplification of spin echoes within a kinetic inductance parametric amplifier, *Science Advances* **9**, eadg1593 (2023).
- [17] C. Eichler, A. J. Sigillito, S. A. Lyon, and J. R. Petta, Electron spin resonance at the level of 10^4 spins using low-impedance superconducting resonators, *Physical Review Letters* **118**, 037701 (2017).
- [18] K. W. Murch, S. J. Weber, C. Macklin, and I. Siddiqi, Observing single quantum trajectories of a superconducting quantum bit, *Nature* **502**, 211 (2013).
- [19] S. J. Weber, A. Chantasri, J. Dressel, A. N. Jordan, K. W. Murch, and I. Siddiqi, Mapping the optimal route between two quantum states, *Nature* **511**, 570 (2014).
- [20] A. Caldwell, G. Dvali, B. Majorovits, A. Millar, G. Raffelt, J. Redondo, O. Reimann, F. Simon, and F. Steffen (MADMAX Working Group), Dielectric haloscopes: A new way to detect axion dark matter, *Phys. Rev. Lett.* **118**, 091801 (2017).
- [21] J. Jeong, S. Youn, S. Bae, J. Kim, T. Seong, J. E. Kim, and Y. K. Semertzidis, Search for invisible axion dark matter with a multiple-cell haloscope, *Phys. Rev. Lett.* **125**, 221302 (2020).
- [22] K. Wurtz, B. Brubaker, Y. Jiang, E. Ruddy, D. Palken, and K. Lehnert, Cavity entanglement and state swapping to accelerate the search for axion dark matter, *PRX Quantum* **2**, 040350 (2021).
- [23] K. M. Backes, D. A. Palken, S. A. Kenany, B. M. Brubaker, S. B. Cahn, A. Droster, G. C. Hilton, S. Ghosh, H. Jackson, S. K. Lamoreaux, A. F. Leder, K. W. Lehnert, S. M. Lewis, M. Malnou, R. H. Maruyama, N. M. Rapidis, M. Simanovskaia, S. Singh, D. H. Speller, I. Urdinaran, L. R. Vale, E. C. van Assendelft, K. van Bibber, and H. Wang, A quantum enhanced search for dark matter axions, *Nature* **590**, 238 (2021).
- [24] S. Barzanjeh, S. Guha, C. Weedbrook, D. Vitali, J. H. Shapiro, and S. Pirandola, Microwave quantum illumination, *Phys. Rev. Lett.* **114**, 080503 (2015).
- [25] S. Barzanjeh, S. Pirandola, D. Vitali, and J. M. Fink, Microwave quantum illumination using a digital receiver, *Science Advances* **6**, eabb0451 (2020), <https://www.science.org/doi/pdf/10.1126/sciadv.abb0451>.
- [26] R. Assouly, R. Dassonneville, T. Peronnin, A. Bienfait, and B. Huard, Quantum advantage in microwave quantum radar, *Nature Physics* **10.1038/s41567-023-02113-4** (2023).
- [27] R. G. Torrome and S. Barzanjeh, Advances in quantum radar and quantum lidar, (2023), [arXiv:2310.07198](https://arxiv.org/abs/2310.07198).
- [28] B. Yurke, Wideband photon counting and homodyne detection, *Phys. Rev. A* **32**, 311 (1985).
- [29] M. Renger, S. Pogorzalek, Q. Chen, Y. Nojiri, K. Inomata, Y. Nakamura, M. Partanen, A. Marx, R. Gross, F. Deppe, and K. G. Fedorov, Beyond the standard quantum limit for parametric amplification of broadband signals, *npj Quantum Information* **7**, 160 (2021).
- [30] T. Yamamoto, K. Koshino, and Y. Nakamura, Parametric amplifier and oscillator based on josephson junction circuitry, in *Principles and Methods of Quantum Information Technologies* (Springer, 2016) pp. 495–513.
- [31] C. Macklin, K. O'Brien, D. Hover, M. E. Schwartz, V. Bolkhovskiy, X. Zhang, W. D. Oliver, and I. Siddiqi, A near-quantum-limited josephson traveling-wave parametric amplifier, *Science* **350**, 307 (2015).
- [32] M. Esposito, A. Ranadive, L. Planat, and N. Roch, Perspective on traveling wave microwave parametric amplifiers, *Applied Physics Letters* **119**, 120501 (2021).
- [33] M. Malnou, M. R. Vissers, J. D. Wheeler, J. Aumentado, J. Hubmayr, J. N. Ullom, and J. Gao, Three-wave mixing kinetic inductance traveling-wave amplifier with near-quantum-limited noise performance, *PRX Quantum*

- 2**, 010302 (2021).
- [34] S. Frasca, C. Roy, G. Beaulieu, and P. Scarlino, Three-wave-mixing quantum-limited kinetic inductance parametric amplifier operating at 6 t near 1 k, *Physical Review Applied* **21**, 024011 (2024).
 - [35] A. Mohamed, E. Zohari, J. J. Pla, P. E. Barclay, and S. Barzanjeh, Selective single- and double-mode quantum-limited amplifier, *Physical Review Applied* **21**, 064052 (2024).
 - [36] M. Xu, R. Cheng, Y. Wu, G. Liu, and H. X. Tang, Magnetic field-resilient quantum-limited parametric amplifier, *PRX Quantum* **4**, 010322 (2023).
 - [37] M. Khalifa, P. Feldmann, and J. Salfi, Kinetic inductance parametric converter, *Physical Review Applied* **22**, 024025 (2024).
 - [38] A. Schneider, T. Wolz, M. Pfirrmann, M. Spiecker, H. Rotzinger, A. V. Ustinov, and M. Weides, Transmon qubit in a magnetic field: Evolution of coherence and transition frequency, *Physical Review Research* **1**, 023003 (2019).
 - [39] L. Planat, R. Dassonneville, J. P. Martínez, F. Foroughi, O. Buisson, W. Hasch-Guichard, C. Naud, R. Vijay, K. Murch, and N. Roch, Understanding the saturation power of josephson parametric amplifiers made from squid arrays, *Physical Review Applied* **11**, 034014 (2019).
 - [40] A. Mohamed and S. Barzanjeh, Path-entangled radiation from a kinetic inductance amplifier, *Phys. Rev. Appl.* **22**, 044055 (2024).
 - [41] S. Chaudhuri, D. Li, K. Irwin, C. Bockstiegel, J. Hubmayr, J. Ullom, M. Vissers, and J. Gao, Broadband parametric amplifiers based on nonlinear kinetic inductance artificial transmission lines, *Applied Physics Letters* **110** (2017).
 - [42] A. Anferov, A. Suleymanzade, A. Oriani, J. Simon, and D. I. Schuster, Millimeter-wave four-wave mixing via kinetic inductance for quantum devices, *Physical Review Applied* **13**, 024056 (2020).
 - [43] J. Zmuidzinas, Superconducting microresonators: Physics and applications, *Annual Review of Condensed Matter Physics* **3**, 169 (2012).
 - [44] N. Kirsh, E. Svetitsky, S. Goldstein, G. Pardo, O. Hachmo, and N. Katz, Linear and nonlinear properties of a compact high-kinetic-inductance WSi multimode resonator, *Phys. Rev. Appl.* **16**, 044017 (2021).
 - [45] D. J. Parker, M. Savytskyi, W. Vine, A. Laucht, T. Duty, A. Morello, A. L. Grimsom, and J. J. Pla, Degenerate parametric amplification via three-wave mixing using kinetic inductance, *Physical Review Applied* **17**, 034064 (2022).
 - [46] Y. Wu, M. Xu, and H. X. Tang, Junction-free microwave two-mode radiation from a kinetic inductance nanowire, *Physical Review Applied* **21**, 014029 (2024).
 - [47] C. Joshi, W. Chen, H. G. LeDuc, P. K. Day, and M. Mirhosseini, Strong kinetic-inductance kerr nonlinearity with titanium nitride nanowires, *Phys. Rev. Appl.* **18**, 064088 (2022).
 - [48] N. Zapata, I. Takmakov, S. Günzler, S. Geisert, S. Ihssen, M. Field, A. Nambisan, D. Rieger, T. Reisinger, W. Wernsdorfer, *et al.*, Granular aluminum parametric amplifier for low-noise measurements in tesla fields, *Physical Review Letters* **133**, 260604 (2024).
 - [49] M. Khalifa and J. Salfi, Nonlinearity and parametric amplification of superconducting nanowire resonators in magnetic field, *Physical Review Applied* **19**, 034024 (2023).
 - [50] L. Zhang, W. Peng, L. X. You, and Z. Wang, Superconducting properties and chemical composition of NbTiN thin films with different thickness, *Applied Physics Letters* **107**, 122603 (2015).
 - [51] V. V. Sivak, S. Shankar, G. Liu, J. Aumentado, and M. H. Devoret, Josephson array-mode parametric amplifier, *Physical Review Applied* (2020).
 - [52] P. Winkel, I. Takmakov, D. Rieger, L. Planat, W. Hasch-Guichard, L. Grünhaupt, N. Maleeva, F. Foroughi, F. Henriques, K. Borisov, *et al.*, Nondegenerate parametric amplifiers based on dispersion-engineered josephson-junction arrays, *Physical Review Applied* **13**, 024015 (2020).
 - [53] C. Eichler, Y. Salathe, J. Mlynek, S. Schmidt, and A. Wallraff, Quantum-limited amplification and entanglement in coupled nonlinear resonators, *Physical Review Letters* **113**, 110502 (2014).
 - [54] E. X. DeJesus and C. Kaufman, Routh-hurwitz criterion in the examination of eigenvalues of a system of nonlinear ordinary differential equations, *Phys. Rev. A* **35**, 5288 (1987).
 - [55] A. B. Pippard and W. L. Bragg, Field variation of the superconducting penetration depth, *Proceedings of the Royal Society of London. Series A. Mathematical and Physical Sciences* **203**, 210 (1950).
 - [56] A. B. Pippard and W. L. Bragg, An experimental and theoretical study of the relation between magnetic field and current in a superconductor, *Proceedings of the Royal Society of London. Series A. Mathematical and Physical Sciences* **216**, 547 (1953).
 - [57] A. J. Annunziata, D. F. Santavica, L. Frunzio, G. Catealani, M. J. Rooks, A. Frydman, and D. E. Prober, Tunable superconducting nanoinductors, *Nanotechnology* **21**, 445202 (2010).
 - [58] S. Frasca, I. N. Arabadzhev, S. B. de Puechredon, F. Oppliger, V. Jouanny, R. Musio, M. Scigliuzzo, F. Minganti, P. Scarlino, and E. Charbon, Nbn films with high kinetic inductance for high-quality compact superconducting resonators, *Physical Review Applied* **20**, 044021 (2023).
 - [59] T.-C. Chien, O. Lanes, C. Liu, X. Cao, P. Lu, S. Motz, G. Liu, D. Pekker, and M. Hatridge, Multiparametric amplification and qubit measurement with a kerr-free josephson ring modulator, *Physical Review A* **101**, 042336 (2020).
 - [60] L. Planat, A. Ranadive, R. Dassonneville, J. P. Martínez, S. Léger, C. Naud, O. Buisson, W. Hasch-Guichard, D. M. Basko, and N. Roch, Photonic-crystal josephson traveling-wave parametric amplifier, *Physical Review X* **10**, 021021 (2020).
 - [61] M. Tinkham, *Introduction to Superconductivity* (McGraw-Hill International Editions, 1996).
 - [62] S. Tripathy, K. Tyagi, and P. Pratap, A comprehensive study of various superconductors for superconducting nanowire single photon detectors applications, *iScience* **27**, 10.1016/j.isci.2024.110779 (2024).